EFFICIENT COMPUTATION AND NEURAL PROCESSING OF ASTROMETRIC IMAGES

Rossella CANCELLIERE

Department of Computer Science
University of Torino
c. Svizzera 185
10149 Torino, Italy
e-mail: `cancelli@di.unito.it`

Mario GAI

National Institute of Astrophysics
Astronomical Observatory of Torino
V. Osservatorio 20
10025 Pino T.se (TO), Italy
e-mail: `gai@oato.inaf.it`

Abstract. In this paper we show that in some peculiar cases, here the generation of astronomical images used for high precision astrometric measurements, an optimised implementation of the DFT algorithm can be more efficient than FFT. The application considered requires generation of large sets of data for the training and test sets needed for neural network estimation and removal of a systematic error called chromaticity. Also, the problem requires a convenient choice of image encoding parameters; in our case, the one-dimensional lowest order moments proved to be an adequate solution. These parameters are then used as inputs to a feed forward neural network, trained by backpropagation, to remove chromaticity.

Keywords: Fourier transform, image analysis, neural network diagnosis

Mathematics Subject Classification 2000: 42, 68, 85

1 INTRODUCTION

The European Space Agency has approved the mission Gaia [1], aimed at a high precision astrometric survey of our Galaxy, for launch in 2011; the Announcement of Opportunity for the data reduction has been issued on November 9, 2006. The mathematical and computing tools used for modern astronomical experiments must meet challenging requirements on resolution and precision, consistent with the measurement goals.

In particular, the location of the diffraction image of an object measured by a real instrument is affected by an apparent displacement, dependent on the source spectral distribution; this effect is called chromaticity [2]; it is described from a mathematical point of view below and clarifications about the state of the art of its effects and about the applied techniques to remove it can be found in [3]. Besides, the formulation of the diffraction integral leads naturally to its implementation based on the Fourier transform (FT).

The image of a star, considered as a point-like source at infinity, and produced by an ideal telescope, with focal length F, an unobstructed circular pupil of diameter D, at wavelength λ, has radial symmetry and is described by the Airy function (1) (see [4] for notation).

$$I(r) = k \left[2 J_1 \left(\pi r D / \lambda F \right) / \left(\pi r D / \lambda F \right) \right]^2 . \tag{1}$$

Here J_1 is the Bessel function of the first kind, order one, k a normalisation constant, and r the radial coordinate on the focal plane. The image has a characteristic size (the Airy diameter) $2.44\lambda/D$.

The use of real telescope, however, produces diffraction images (hereafter called real images) described by the square modulus of the FT of the pupil function $e^{i\Phi}$ and caracterized by a set of aberration values that depend on the phase aberration Φ:

$$I(r, \phi) = \frac{k}{\pi^2} \left| \int d\rho \int d\theta \, \rho \, e^{i\Phi(\rho,\theta)} e^{-i\pi r \rho \cos(\theta - \phi)} \right|^2 \tag{2}$$

where $\{r, \phi\}$ and $\{\rho, \theta\}$ are the radial coordinates on image and pupil plane, respectively, and the integration domain corresponds to the pupil: for the circular case, $0 \le \rho \le 1$; $0 \le \theta \le 2\pi$. In case of a rectangular pupil, it is more convenient to use Cartesian coordinates on both image and pupil plane, e.g. $\{x, y\}$ and $\{\xi, \eta\}$ integrated between the appropriate boundaries.

The phase aberration Φ describes for the real case the deviation from the ideal flat wavefront, i.e. the wavefront error (WFE), and is usually decomposed by means of the Zernike functions ϕ_n ([4]):

$$\Phi(\rho, \theta) = \frac{2\pi}{\lambda} \text{WFE} = \frac{2\pi}{\lambda} \sum_{n=1}^{21} A_n \phi_n(\rho, \theta). \tag{3}$$

If $\Phi = 0$ (non-aberrated case, $\{A_n\} = 0$), we obtain a flat wavefront, i.e. WFE = 0, and Equation (1) is retrieved for the circular pupil.

The WFE itself is independent from wavelength, but wavelength dependence in the pupil function is induced by the $2\pi/\lambda$ factor. Also, the nonlinear relationship between the set of aberration coefficients A_n and the image is put in evidence by replacement of Equation (3) in Equation (2).

The FFT algorithm associates the resolution in one of the domains to the full range of the corresponding conjugate variable; besides, the diffraction integral is physically limited to the real pupil size. Therefore, the simplest implementation generates just two points over the characteristic length of the system, which is clearly not sufficient to provide an acceptable image detail. A typical approach to overcome this limitation consists in a formal extension of the pupil domain to a much larger size, to achieve the desired resolution, provided the function used as argument is set to zero in the extended interval. Besides, this approach involves a significant amount of computation, required from the formal definition, over quantities set to zero. This consideration led us to test the alternative approach of direct computation of the DFT in its original formulation derived from discretization of the Fourier integral.

The number of points used to evaluate the discrete Fourier transform by FFT is, however, crucial, because of its impact on both resulting precision and required computational effort; in this paper we present a method that allows usage of a number of points suitable to the desired resolution, reducing at the same time the computational cost with respect to the classic FFT algorithm.

Because the real polychromatic image of an unresolved stellar source is produced by integration over the appropriate bandwidth of the monochromatic PSF above, it is evident that objects with different spectral distributions have different image profiles; this fact implies that the position estimate produced by any location algorithm (e.g. the centre of gravity, COG), evaluated on the image profile itself, is affected by discrepancy with respect to the nominal position generated by an ideal optical system.

The location estimate is sensitive to the algorithm used [5], in case of discrepancies between the real signal and its expected profile, so that it is crucial to model the instrument and maintain its calibration with high precision. The chromaticity can be minimized by instrument design and construction [2], but the residual chromaticity must be taken into account in the data reduction phase. In this paper therefore our aim is the diagnosis of chromaticity that affects images which are realistic in the sense of a signal profile variation compatible with our expectations on the imaging quality of the instrument. Besides, at this stage we do not address the effects of random noise, since we feel necessary to identify clearly the limiting performance with respect to systematic errors. The realistic range of image variation is achieved by selection of the aberration range (in Section 3); the PSFs are not affected by readout or photon noise.

In past works [6] we developed a method for Seidel aberration estimate from the focal plane images, but the greater number of aberration terms to be detected in the Zernike decomposition would require a huge increase in the data set of examples for proper training, making the computational effort unbearable. Therefore, here we study how to identificate chromaticity from the image profile itself, using

the diagnosis capability of a neural network (NN) properly trained. Our choice is due to the existence of different works concerning the use of NN in astronomical adaptive optics (see [7, 8]) where NN always demostrated great robustness to noise and damages and powerful capabilities of flexible learning.

Real-world image processing systems frequently represent a chain of hierarchically organized, interacting components ranging from basic preprocessing to high-level image analysis and interpretation. Functional operations such as preprocessing, feature extraction, data reduction/compression segmentation, object recognition, image understanding, and scene analysis have to be applied to different structural levels of data complexity ranging from pixel data, local features, structure and texture level data to objects, object arrangements, scene and context description. Neural networks, as a special kind of learning and self-adapting data processing system, have to offer considerable contributions to this field. Their abilities to handle noisy and high-dimensional data, nonlinear problems, large data sets etc. have led to a wide scope of successful applications in digital image processing. A very interesting survey on this theme can be found in [9].

Other interesting works can be found in literature about neural network capabilities to solve diagnosis, recognition or classification tasks in the framework of image processing: problems concerning character recognition ([10]), image processing in medical applications ([11]), image compression ([12]), and so on.

A very interesting application concerns the use of cellular neural networks (CNN); CNN are members of the hardware family called vision chips. Based on state-of-the-art technology, a vision chip is defined as a VLSI chip that can perform image processing tasks. The theory of CNN develops in two main fields: cellular automata and neural networks; as an interdisciplinary product, CNN utilizes cellular hardware structures to gain ultrahigh image processing speed ([13]).

The paper is organized as follows: in Section 2 we discuss the Fourier transform computation, comparing the proposed technique with the classical fast Fourier transform algorithm, and we present the image encoding method. In Section 3 we describe the generation of the data sets and in Section 4 we resume the main features of sigmoidal NN and backpropagation algorithm, with a brief reminder of the specific definitions, then we discuss the data processing and the obtained results.

2 FOURIER TRANSFORM COMPUTATION
AND DIFFRACTION IMAGE ENCODING

In this section we describe the generation of the Fourier transform and the identification of convenient parameters for encoding of realistic images (as expected from real telescopes), according to Equation (2).

2.1 Discrete Fourier Transform

There are many science applications for which an accurate Fourier transform of the signal is necessary. For example, to achieve the frequency spectrum $X(\omega)$ of a time

dependent signal $x(t)$, sampled at N time instants t_n (i.e. the signal has a finite duration, with N contiguous nonzero samples), the Discrete Fourier Transform (DFT) is:

$$X(\omega) = \sum_{n=0}^{N-1} x(t_n) exp(-j\omega t_n). \tag{4}$$

Frequently, the sampling is uniform ($t_n = n\Delta T$; $x(t_n) = x(n)$), so that Equation (4) becomes:

$$X(\omega) = \sum_{n=0}^{N-1} x(n) exp(-jn\omega\Delta T), \tag{5}$$

where T is the sampling period. Usually $X(\omega)$ is also evaluated at a set of N points ω_n, often evenly spaced ($\omega_n = n\omega_0$). A natural choice of frequency values is $\omega_n = 2\pi n/N$, ($n = 0 \ldots N-1$), so in terms of real frequencies we have a resolution of $\Delta\omega = 2\pi/(NT)$ or $\Delta f = 1/(NT)$.

Throughout the following sections of this paper, we retain the uniform sampling notation for ease of comparison with the FFT case; however, we do not use further specializations of the algorithm, such as the Goertzel methods (see [14]), because it is restricted to this condition, whereas in our future applications non-uniform sampling may be required.

The frequency sampling can be modified e.g. by adding extra zeros to the signal [15]; if we want to multiply by M the frequency resolution we can add $(M-1)N$ zeros in the sequence $x(n)$, thus obtaining a new sequence of length $K = NM$. The alternative of simple interpolation of the FFT output is often acceptable, but the choice requires caution with respect to the effective information content (signal resolution and duration), and to the possible introduction of artefacts.

If we assume $M = N$, for simplicity, the zero-padding approach is associated to a computational cost for the usual FFT algorithm of order of $K \log K = N^2 \log(N^2)$, against order of $K^2 = N^4$ for standard DFT. However, in many applications it is necessary to achieve a higher resolution within a small frequency interval only, which makes convenient the evaluation of the DFT by direct matrix multiplication (hereafter, DFT *tout-court*). Actually, in this case, the computational cost for the Fourier transform of N samples for N frequency values in a given interval is N^2, i.e. smaller than the above cost of the FFT algorithm by a factor $\log(N^2)$. It should be noted that the FFT cost estimate is valid when the data size is a power of two, and the actual computation time is extremely variable depending on data factorisation, and therefore on the implementation.

Moreover, since we deal with two-dimensional images, the computational cost of the Fourier Transform evaluation increases for both methods. Assuming simple repetition of either one-dimensional FT algorithm, or for N^2 (FFT) and N (DFT) times, the computational cost becomes of order of $N^2 \log(N^2) \times N^2$ for FFT and $N^2 \times N$ for DFT by direct matrix multiplication. The practical implementation can be further optimised, of course; besides, the estimate is valid only within the computation-limited regime, and for any real computer, at increasing size of the processed arrays, the case becomes input/output-limited, when the physical memory

is saturated and the virtual memory mechanisms start swapping data towards the mass storage devices.

We verify these considerations by performing FT evaluation by both FFT and DFT, on square format images, over the range $10 \leq N \leq 65$ points. Since the actual image format for the FFT size is N^4, the largest array considered is $4K \times 4K$, i.e. 16 mega-pixels. At this point, our desktop computers already have a significant virtual memory access.
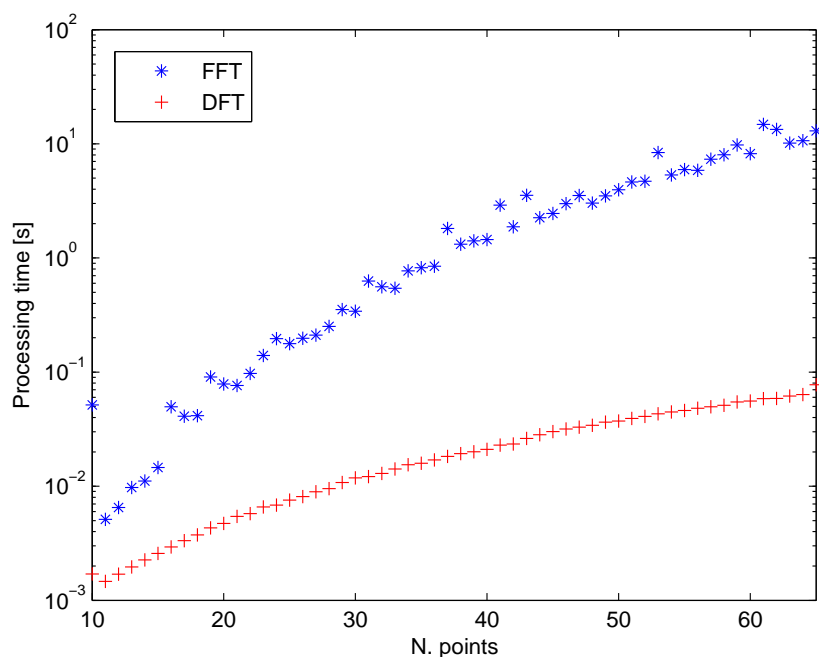

Fig. 1. Processing time comparison: direct matrix multiplication is always faster

In Figure 1, we plot the FFT and DFT processing times as functions of N, showing that direct matrix multiplication is always faster.

In Figures 2 and 3, each curve is shown together with its theoretical fitting function, i.e. αN^3 and $\beta N^4 \log(N^2)$, where α and β are two constants.

2.2 Image encoding

To maximise the field of view, i.e. to observe simultaneously a large area on a given size detector, typical astronomical images are sampled over a small number of pixels. Typical sampling requirements, related to the Nyquist-Shannon criterion, are of order of two pixels over the full width at half maximum, or about five pixels within
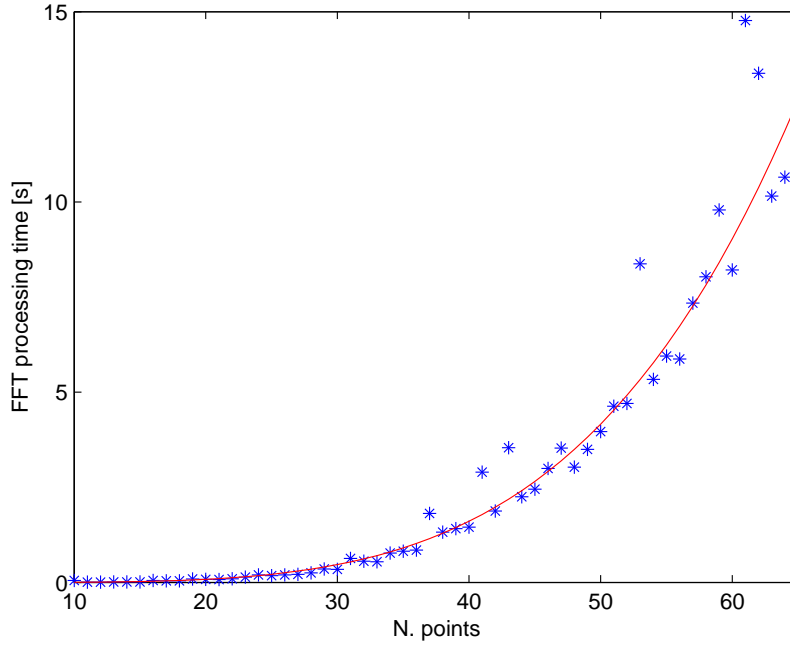
Fig. 2. Experimental processing times (dots) and theoretical fitting curve for FFT

the central diffraction peak. The detected signal is then affected by significant variation depending on the phase of the pixel array with respect to the photon distribution. The pixel values are then not convenient for direct evaluation of the discrepancy of the effective image with respect to the nominal case, and suitable descriptors are to be identified.

Higher sampling resolution would minimise the effects of the finite pixel size [5], at the expense of the field of view, which is not acceptable. Besides, even in case of well sampled images, usage of a large number of pixels as input to the NN is impractical, because of the large computational load involved. We then identify a more compact encoding that allows extraction of the desired information for chromaticity diagnosis. Each input image is described by the centre of gravity (and a few low order central moments) according to the definitions

$$\mu_y = \sum_n y_n \cdot I_n / I_{int}$$

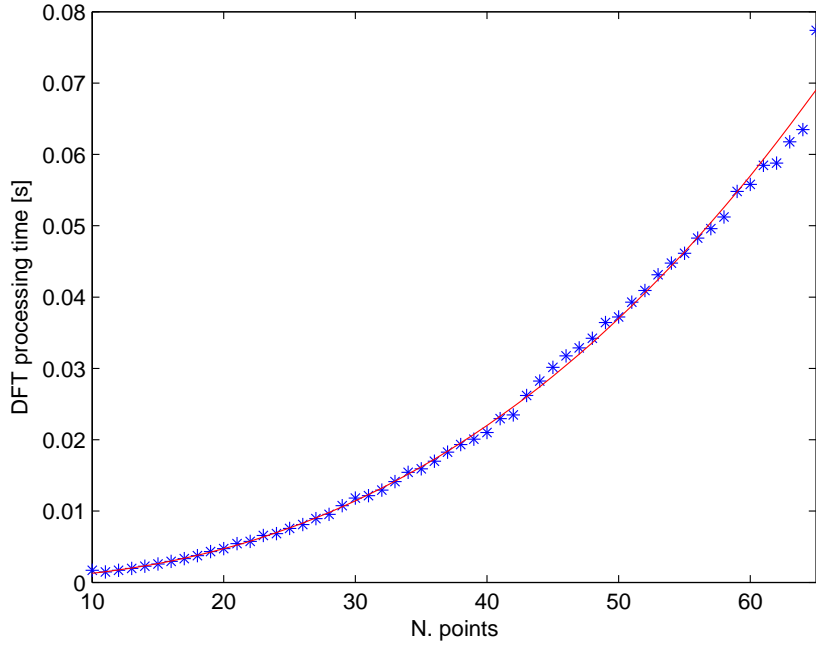$$\sigma_y^2 = \sum_n (y_n - \mu_y)^2 \cdot I_n / I_{int} \tag{6}$$

Fig. 3. Experimental processing times (dots) and theoretical fitting curve for DFT

$$M(j) \quad = \quad \sum_n \left(\frac{y_n - \mu_y}{\sigma_y} \right)^j \cdot I_n \,/\, I_{int}, \quad j > 2$$

where $I_{int} = \sum_n I_n$ is the measured photometry. We adopt a weighted version of the real images, described in Equation (2), multiplying them by the detected non-aberrated image; so doing we provide better performances in cases affected by photon noise and add effectiveness to treatment of realistic data [5].

The Gaia measurement [1] is mainly one-dimensional: most images are integrated in the low resolution direction for telemetry reasons. Thus the signals (I_n) are also reduced to one dimension, y in the Gaia convention. One-dimensional encoding is a further change with respect to previous investigations [6], in which we took advantage of the full two-dimensional image structure to estimate the aberration terms. The moments in the low resolution direction were verified to have negligible effect on chromaticity. It is then possible to use simple combinations of the standard one-dimensional measurements for processing.

The central moments are much less sensitive than individual intensity values to the effects related to pixel size and phase. Thus, they can be computed conveniently also from the detected low resolution images. The usage of moments as NN inputs for image profile description is discussed in more detail in [16].

3 DATA SETS GENERATION

In this section we describe the generation of the training and test sets and the identification of the most convenient image parameters.

With respect to our previous work on chromaticity (see [3]), the current simulation takes into account a number of realistic instrument contributions, although some still in a simple form. In general, such terms have the effect of reducing the image sharpness, which in turn reduces both the chromaticity and the signature on the moments. It is therefore important to verify whether the principle of chromaticity estimation from the moments still holds, also in the case of more realistic images, and to evaluate the impact on the performance. In practice, the relationship between chromaticity and some critical moments might be degraded significantly, or the number of cases required for proper NN training might increase to unmanageable levels.
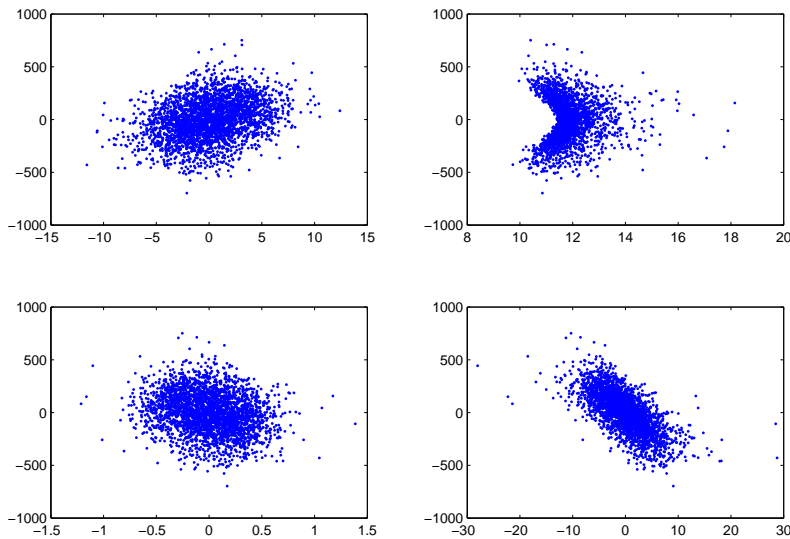

Fig. 4. From top to bottom: distribution of chromaticity vs. image centre of gravity, RMS width, third and fifth order moments

We verify that the relationship between chromaticity and moments remains good (see Figure 4); also, in the neural processing results we verified that the performance on the test set significantly improves, thus allowing us to avoid the pre-processing previously necessary ([3]).

The spatial resolution on the focal plane (previously $2\,\mu$m on each coordinate) is improved to $1\,\mu$m in the along scan direction, and relaxed to $6\,\mu$m in the across

scan direction (much less critical), compatibly with basic sampling requirements and computing time optimisation. Also, the computation is restricted to the region of interest corresponding to the planned readout windows (with margins).

The spectral representation has also been improved with respect to the previous monochromatic case. The polychromatic images are built by superposition of monochromatic PSFs, weighed with a distribution centred on the effective wavelengths 787 nm and 617 nm, estimated for blackbody sources at 3 000 K (red) and 30 000 K (blue), with FWHM of 200 nm, considered representative of the overall instrument and detector response. The basic parameters of the Gaia telescope (aperture, focal length) are used.

Notably, using the standard FFT approach, the sampling in either pupil or focal plane is variable with respect to wavelength, which is not physically sound. In our previous experiment, the focal plane sampling was retained, to avoid the need for image interpolation, thus inducing wavelength dependent sampling of the WFE corresponding to the current aberration case.

Realistic degradations due to nominal detector (finite pixel size and clocking in time-delayed integration) are taken into account, by filtering the PSF through representative functions. In the current approximation, the latter are rectangles with constant value over a width associated to the pixel size ($10\,\mu$m) and the four-phase clocking ($5\,\mu$m). Further realistic contributions (e.g. the modulation transfer function) can be easily introduced in future developments.

The polychromatic PSF for each source case is then integrated in the across scan direction (implementing the planned binning readout), and the one-dimensional moments are computed, for later neural processing. The chromaticity is estimated as COG difference between the blue and red star images.

A set of aberration cases is generated, in the regime of small image degradation, i.e. of reasonably good imaging performance. The Zernike aberration coefficients are generated from a Gaussian random distribution with $\sigma = 50$ nm for each component. The coefficient range is not configuration specific, but covers a set of mathematically possible cases, larger than the physically feasible optical systems. The corresponding RMS WFE on the aperture, averaged over the data set, is about 50 nm. The sample considered is thus representative of a range of realistic optical configurations.

Some of the moments do not have a significant trend with respect to chromaticity, and can therefore be neglected. The moment selection was verified on the NN using a pruning technique, i.e. selectively removing some of them and checking the convergence, until reaching the minimum number of parameters compatible with good training.

The NN inputs are thus defined in terms of the local instrument response, expressed by the local aberration values, then encoded in the moments for red and blue sources, which can be considered one as the reference and the other as the generic star of known spectral type. In particular, the COG of the reference object is the deviation of the image position with respect to an ideal system, and it is associated to the classical distortion; therefore, it is a system property which can be calibrated
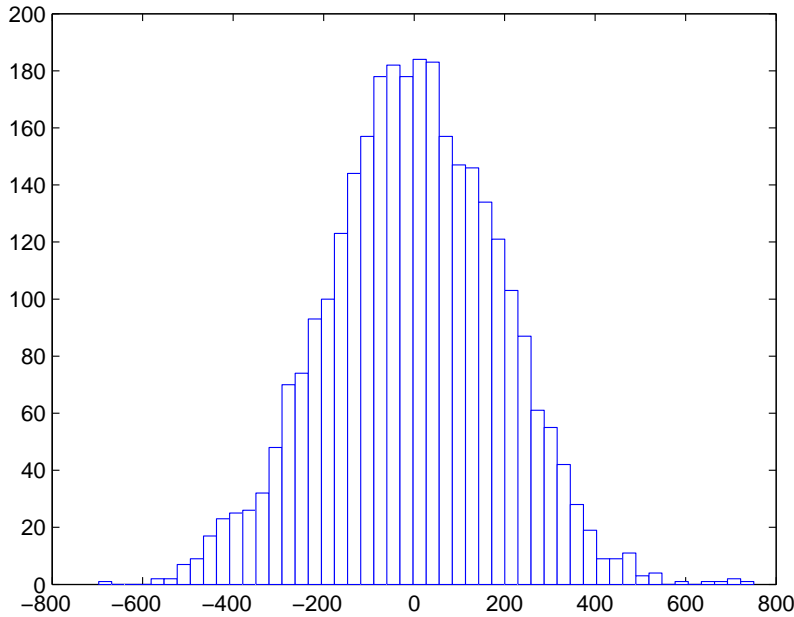
Fig. 5. Histogram of the distribution of test set input chromaticity

from the science data. The other inputs from the reference source are the image RMS width, the third and the fifth order moments. The inputs associated to the measured signal, from a star of different, known spectral type, are the third and fifth order moments.

The histogram of input chromaticity distribution in the test set is shown in Figure 5, and it is approximately Gaussian.

4 NEURAL PROCESSING AND RESULTS

Neural networks learn from examples; that is, given the training set of N multi-dimensional data pairs $\{(x_i, F(x_i))/x_i \in \Re^P, F(x_i) \in \Re^Q\}$, $i = 1, \ldots, N$, after the training if x_i is the input to the network, the output is close to, or coincident with, the desired answer $F(x_i)$ and the network has generalization properties too, that is it gives as output $F(x_i)$ even if the input is only "close to" x_i, for instance a noisy or distorted or incomplete version of x_i; a comprehensive review on NN properties and applications can be found in [17].

In our work we use the multilayer perceptron, first introduced in 1986 (see [18]), as an extension of the perceptron model [19].

The multilayer perceptron, with sigmoidal units in the hidden layers, is one of the most known and used NN models: it computes distances in the input space using a metric based on inner products and it is usually trained by the backpropagation algorithm. The architecture of a sigmoidal NN is schematically shown in Figure 6, in which we find the most common three-layers case.
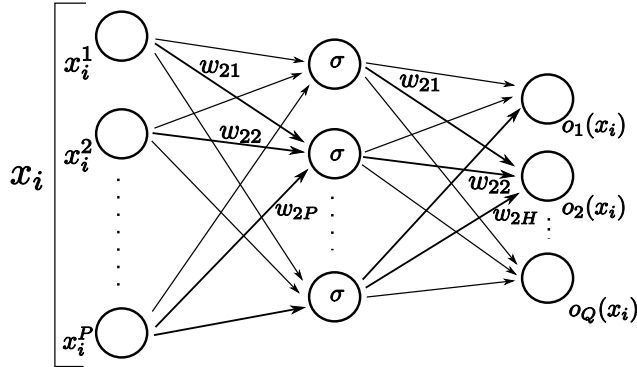

Fig. 6. Sigmoidal neural network with one hidden layer

The network is described by Equation (7):

$$a_j^{k+1} = \sum_{j'} w_{jj'} o_{j'}^k + bias_j$$
$$o_j^{k+1} = \sigma(a_j^{k+1}) \equiv \frac{1}{1+e^{-a_j^{k+1}}} \qquad (7)$$
$$o_m^{out} \equiv \sum_j w_{mj} o_j^{out-1}.$$

Here a is the input to each unit, o is its output and w_{ij} is the weight associated to the connection between units i and j; each unit is defined by two indexes, a superscript specifying its layer (i.e. input, hidden or output layer) and a subscript labelling each unit in a layer.

The training procedure is finalized to find the best set of weights $\{w_{ij}\}$ solving the approximation problem $o(x_i) \approx F(x_i)$ and this is usually reached by the iterative process corresponding to the standard backpropagation algorithm.

At each step, each weight is modified accordingly to the gradient descent rule (a more detailed description can be found in [18]), completed with the momentum term, $w_{ij} = w_{ij} + \Delta w_{ij}$, $\Delta w_{ij} = -\eta \frac{\partial E}{\partial w_{ij}}$ where E is the error functional defined above. This procedure is iterated many times over the complete set of examples $\{x_i, F(x_i)\}$ (the training set), and under appropriate conditions it converges to a suitable set of weights defining the desired approximating function.

Convergence is usually defined in terms of the error functional, evaluated over the whole training set; when a pre-selected threshold E_T is reached, the NN can be tested using a different set of data $\{x_i', F(x_i')\}$, the so called test set.

We use a sigmoidal NN with five inputs describing each blue and red star image plus the blue COG, one output (the chromaticity), and a single hidden layer with 30 units. The NN is trained by 10 000 iterations on a training set made by 10 000 instances, and its performance is verified on the 3 000 instances of the test set; in particular, the discrepancy between the NN output (estimated chromaticity) and target (actual chromaticity for the test set data instances) can be considered as the $r$esidual chromaticity after correction obtained from the NN results.

	Input Chromaticity	Residual Chromaticity (with outliers)	Residual Chromaticity (without outliers)
	[nm]	[nm]	[nm]
Min.	−697.25	−66.76	−13.83
Mean	−1.20	−2.49	−2.51
Max.	750.62	153.29	9.253
RMS	190.50	4.08	1.91

Table 1. Main parameters of input and residual chromaticity in test set

The main statistical parameters of the residual chromaticity distributions, compared with the corresponding values of nominal chromaticity distribution (test set), are listed in Table 1. The central column refers to the diagnosis performances with outliers, i.e. on the whole test set; we noted, however, that on some values the so called outliers (18 instances, 0.6 % of data) performances are not so good, and they are outside the $\pm 3\sigma$ interval. This problem will be the object of future works devoted to better understand this difficulty; however, we evaluated again the residual cromaticity distribution without these values obtaining the diagnosis performances listed in the right column; this distribution is shown in Figure 7. The 99.4 % of originally processed data is, however, within the $\pm 3\sigma$ interval.

Since the goal is the computation of output values coincident with the predefined target values, the plot of output vs. target, shown in Figure 8, should be ideally a straight line ($y = a + bx$) at angle $\pi/4$, passing for the origin, i.e. with parameters ($a = 0$, $b = 1$).

We compute the best fit parameters of the NN output vs. target distribution and their standard deviation; the results, shown in Table 2, are quite consistent with the expectations.

Offset	$a = -2.498 \pm 0.074$
Slope	$b = 0.998 \pm 3.9e{-}004$

Table 2. Main parameters and errors of the linear fit

5 CONCLUSIONS

In this paper we use a neural network to diagnose and correct the systematic astrometric error of chromaticity, in a framework consistent with the mission Gaia
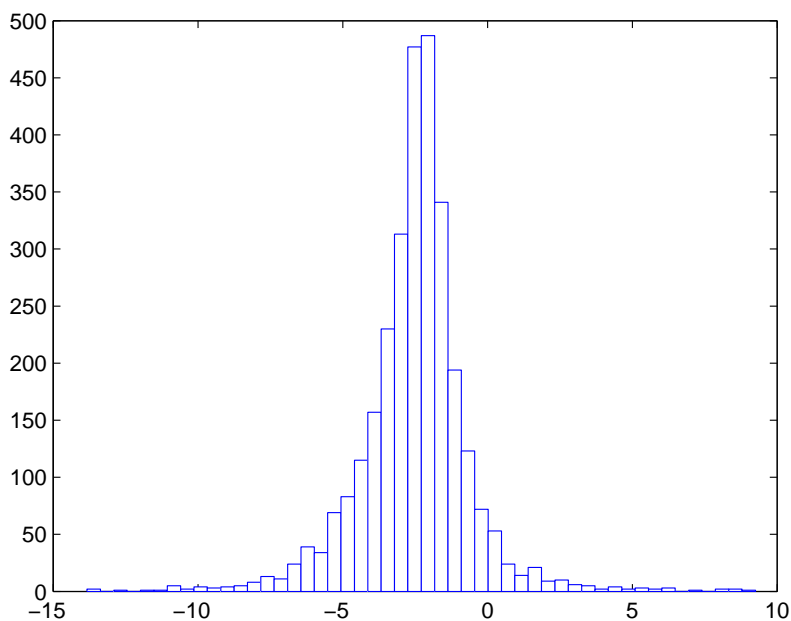
Fig. 7. Histogram of the distribution of test set residual chromaticity

measurements. The science data are efficiently encoded in a set of low order image moments. The NN, with 300 internal nodes, is trained on a set of 8 000 data instances, and evaluated on a test set of 2 000 cases.

The NN diagnostics on the test set appears to be quite effective, as the residual chromaticity distribution, after data correction based on the NN results, is greatly reduced with respect to the initial distribution (Table 1).

Applying the NN output for correction of the chromaticity on the Gaia measurements, we may expect a significant reduction of the associated error; also, the residual chromaticity is expected to be random.

Future developments will include evaluation of the sensitivity to measurement noise, propagated through the image moments, which will induce practical limitations to the correction effectiveness, depending on the source brightness.

From the current results, NN diagnostics used to greatly reduce the chromatic error on astrometric measurements appears to be a tool able to produce effective results.
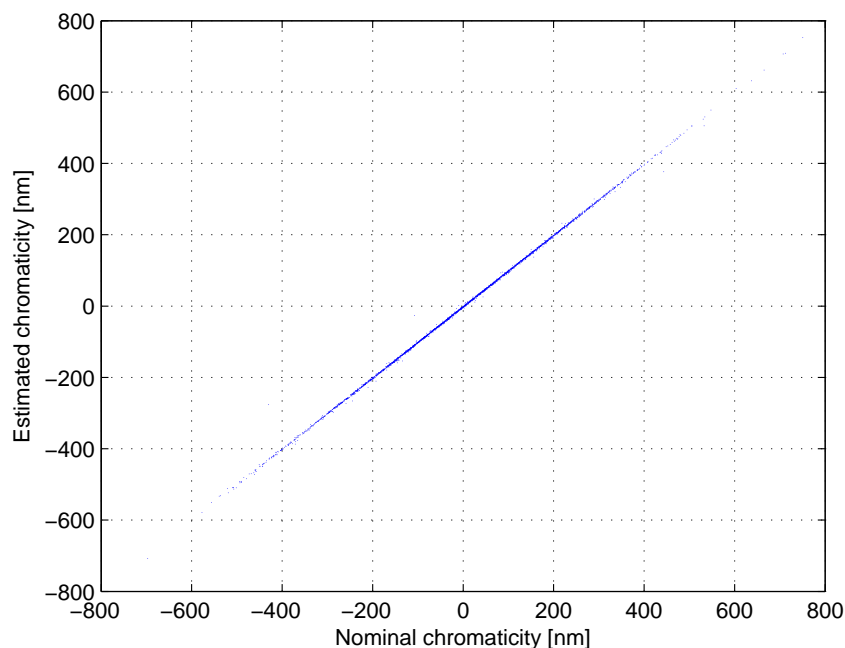
Fig. 8. Output vs. target distribution of chromaticity values over the test set

REFERENCES

[1] PERRYMAN, M. A. C. et al.: GAIA – Composition, Formation and Evolution of the Galaxy. Concept and technology study, Rep. and Exec. Summary, ESA-SCI, (2000) 4, European Space Agency, Munich, Germany 2000.

[2] BUSONERO et al.: Chromaticity in All-Reflective Telescopes for Astrometry. Astronomy and Astrophysics, Vol. 449, 2006, No. 2, pp. 827–836.

[3] CANCELLIERE, R.—GAI, M.: Neural Network Correction of Astrometric Chromaticity. Mon. Not. R. Astron. Soc., Vol. 362, 2005, No. 4, pp. 1483–1488.

[4] BORN, M.—WOLF, E.: Principles of Optics. Pergamon, New York 1985.

[5] GAI, M.—CASERTANO, S.—CAROLLO D.—LATTANZI, M. G.: Location Estimators for Interferometric Fringes. Publ. Astron. Soc. Pac., 1998, 110, p. 848.

[6] CANCELLIERE, R.—GAI, M.: Neural Network Performances in Astronomical Image Processing. Proceedings of the 11th European Symposium on Artificial Neural Networks (ESANN 2003), Bruges (Belgium), April 23–25, 2003, p. 515.

[7] LOYD-HART, M.—WIZINOWICH, P.—MCLEOD, B.—WITTMAN, D.—COLUCCI, D.—DEKANY, R.—MCCARTHY, D.—ANGEL, J. R. P.—SANDLER, D.:

First Results of an On-line Adaptive Optics System with Atmospheric Wavefront Sensing by an Artificial Neural Network. ApJ, Vol. 390, 1992, pp. L41–44.

 [8] WIZINOWICH, P.—LOYD-HART, M.—ANGEL, R.: Adaptive Optics for Array Telescopes Using Neural Networks Techniques on Transputers. Transputing '91, IOS Press, Washington D. C., Vol. 1, 1991, pp. 170–183.

 [9] WISMULLER, A.—SEIFFERT, U.: Digital Image Processing With Neural Networks. Proceedings of the 11th European Symposium on Artificial Neural Networks (ESANN 2003), Brugges (Belgium), April 23–25, 2003, p. 493.

[10] WANG, M. et al.: Character Recognition by Synergic Neural Network Based on Selective Attention Parameters. Proceedings of IST/SPIE's 15th Annual Symposium "Electronic Imaging", January 20–24, 2003, Santa Clara, California, USA.

[11] WARE, J. A.—CIUCA, I.: A Neural Network Based Integrated Image Processing Environment for Object Recognition in Medical Applications. 10th IEEE Symposium on Computer-Based Medical Systems (CBMS '97), 1997, p. 149.

[12] WANG, L.—OJA, E.: Image Compression by MLP and PCA Neural Networks. In 8th Scandinavian Conference on Image Analysis, 1993, p. 1317.

[13] YANG, T.: Cellular Neural Networks and Image Processing: The Science of Cellular Local Rules. Nova Publishers, 2002.

[14] BURRUS, C. S.–PARKS, T. W.: DFT/FFT and Convolution Algorithms, Theory and Implementation. John Wiley and Sons, 1985.

[15] HOLLOS, S.—HOLLOS, R.: C Program Magnifies Spectrum When an FFT Can't Hack It. Electronic Design Online ID No. 5575, 2003.

[16] CANCELLIERE, R.—GAI, M.: A Comparative Analysis of Neural Network Performances in Astronomy Imaging. Applied Numerical Mathematics, Vol. 45, 2003, No. 1, p. 87.

[17] HAYKIN, S.: Neural Networks: A Comprehensive Foundation. IEEE Computer Society Press, 1994.

[18] RUMELHART, D.—HINTON, G. E.—WILLIAMS, R. J.: Learning Internal Representation by Error Propagation. In Parallel Distributed Processing (PDP): Exploration in the Microstructure of Cognition, MIT Press, Cambridge (Massachussetts), Vol. 1, 1986, p. 318.

[19] MINSKY, M.—PAPERT, S.: Perceptrons. MIT Press, Cambridge, MA, 1969.

Rossella CANCELLIERE graduated with a Laurea in physics at the University of Torino (Italy), summa cum laude, in 1991. She was with several industries and academic research institutes, such as Polytechnic of Torino, Cselt (Torino), and University of Milano, where she took her Ph. D. in computational mathematics and operations research. Since October 1999 she is researcher at the University of Torino and since 2005 she is at the Department of Computer Science of the same university, where she works in the machine learning and data mining fields. Lecturer for the course of Neural Networks at the University of Torino since 2004.
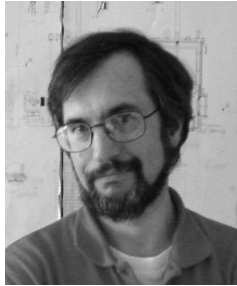
Mario GAI graduated with a Laurea in physics at the University of Torino (Italy), summa cum laude, on March 16th, 1989. Since 1991 he is research astronomer at the Osservatorio Astronomico di Torino. Main activities: design, integration and characterisation of near and thermal infrared cameras for astronomy; design, conceptual test and performance analysis of astronomical instrumentation for interferometry from ground (LBT, VLTI) and high precision astrometry from space (ESA mission GAIA). Lecturer for the course of Laboratory of Astrophysics at the University of Torino in the period 2002–2006.